

Ultrahigh continuous-wave intensities in high-NA optical cavities through suppression of the parametric oscillatory instability

L. Maisenbacher,* A. Singh,* I. M. Pope, and H. Müller
Department of Physics, University of California, Berkeley, Berkeley, USA
 (Dated: March 2, 2026)

Ultrahigh continuous-wave intensities ($>300 \text{ GW/cm}^2$) in high-NA optical cavities enable applications from phase-contrast electron microscopy to ultradeep dipole traps for molecules. However, the intensity can be limited by the parametric oscillatory instability (PI), where mirror vibrations scatter light from one cavity mode into another. We observe PI in a table-top Fabry-Pérot cavity, show that the mechanical modes are MHz-frequency bulk acoustic modes inside the mirrors, and measure their Q factor. By using low- Q mirrors, we achieve $>500 \text{ GW/cm}^2$ intensities in an open, free-space cavity.

Introduction.—Optical cavities with high intracavity power and numerical aperture ($\text{NA} > 0.01$) are an emerging technology that enables ultrahigh continuous-wave intensities ($>300 \text{ GW/cm}^2$) [1]. Pioneered for use as a laser phase plate for electron microscopy [2–4], such cavities may be used for coherent electron beam manipulation [5] or as ultradeep ($>1 \text{ K}$) optical dipole traps for molecules [6]. Their intensities are enabled by careful management of thermal effects through low-expansion mirror substrates and low-absorption, low-defect mirror coatings [1, 4]. As we show here, the radiation pressure acting on the mirrors can likewise limit the intracavity intensity through the parametric oscillatory instability (PI) [7]. PI occurs when a nascent excitation of a mechanical mode of a mirror, possibly generated by thermal fluctuations, is amplified by light circulating in the driven mode of the optical cavity [8]. If the mechanical mode is resonant with the frequency difference between the driven mode and a higher-order optical mode and has spatial overlap with both modes, light from the driven mode is Stokes-scattered into the higher-order mode by mirror vibrations. The resulting beating between the two optical modes modulates the radiation pressure, which then further drives the mechanical mode, closing the feedback loop. When the power in the driven mode exceeds a threshold, the parametric gain of this process exceeds unity, and energy is transferred from the driven mode into the higher-order mode and the mirror vibration, ultimately clamping the driven mode’s power at the threshold.

PI has been observed in micro-mechanical oscillators [9, 10], in km-long arm cavities of gravitational wave detectors [11], and in purpose-built cavities incorporating intracavity oscillators [12–14]. Here, we report what is, to our knowledge, the first observation of PI in a tabletop Fabry-Pérot optical cavity. The cavity is symmetric and near-concentric, $L \approx 100 \text{ mm}$ in length, and consists of two $R = 50 \text{ mm}$ radius of curvature mirrors made from ultra low expansion glass (ULE) [15] (Fig. 1 (a)). It operates in vacuum at a wavelength of $\lambda = 1064 \text{ nm}$ with circulating powers up to $\approx 100 \text{ kW}$. We interferometrically observed that each mirror forms a stable acoustic

cavity, whose modes interact with the optical modes at MHz frequencies, in contrast to the surface modes observed in [11, 12]. We derived the corresponding theory and find good agreement with the experimental data. These data also allowed us to determine the previously unmeasured Q factor ($\approx 10^5$) of ULE at MHz frequencies. Finally, we replaced the ULE mirrors with Zerodur

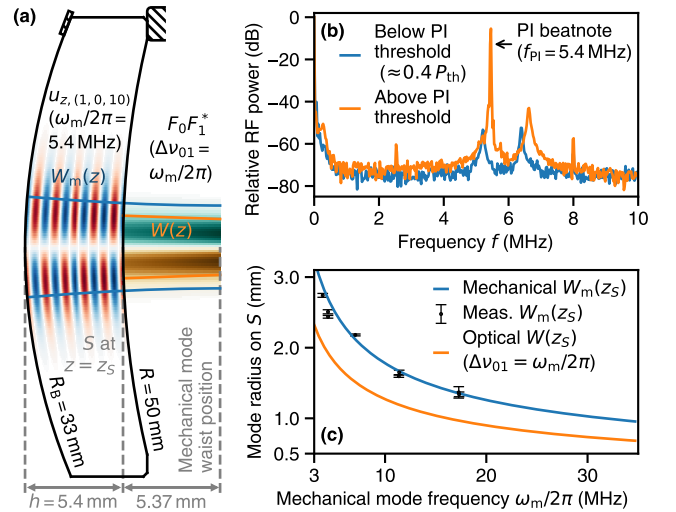


FIG. 1. (a) Cross-sectional view of cavity mirror, held by flexure-mounted pads (hatched, one of three shown). The displacement u_z of the $(m, n, p) = (1, 0, 10)$ mechanical mode, with a frequency of $\omega_m/(2\pi) = 5.4 \text{ MHz}$, is shown in blue for positive and in red for negative displacements. The beatnote amplitude $F_0 F_1^*$ of the driven and higher-order optical modes for transverse mode spacing $\Delta\nu_{01} = \omega_m/(2\pi)$ is also shown (green/orange for positive/negative amplitude). (b) RF power spectrum of cavity transmission photodetector with circulating power below (blue) and above (orange) PI threshold. A weak laser sideband at frequency f was applied to show the transverse mode spectrum of the (astigmatic) optical cavity. Data from ULE mirror set 2; 10 kHz resolution bandwidth. (c) Calculated (blue line) and measured (black circles) mechanical mode radii $W_m(z_S)$ and calculated optical mode radii $W(z_S)$ (orange line; for $\Delta\nu_{01} = \omega_m/(2\pi)$) at mirror front surface S and versus $\omega_m/(2\pi)$. Error bars show 1σ uncertainty.

glass-ceramic mirrors whose lower Q factor suppressed PI sufficiently to allow us to demonstrate intensities in excess of 500 GW/cm².

Theory.—We assume the TEM_{00,(q)} optical mode (q : longitudinal index), containing circulating power $P_{\text{circ},0}$, as the driven mode and the TEM_{10,(q-1)} optical mode as the higher-order mode, where TEM_{mn,q} are Hermite-Gaussian (HG) modes (m, n : transverse indices). The PI parametric gain for a mechanical mode with index j is $P_{\text{circ},0}/P_{\text{th},j}$ [11], where $P_{\text{th},j}$ is a power threshold. The mechanical mode's exponential decay time is

$$\tau_{m,j} = 1/[\gamma_{m,j}(1 - P_{\text{circ},0}/P_{\text{th},j})], \quad (1)$$

with the mechanical amplitude decay constant $\gamma_{m,j}$. When $P_{\text{circ},0}$ exceeds $P_{\text{th},j}$, PI occurs ($\tau_{m,j} < 0$), and the mechanical mode amplitude grows exponentially. $P_{\text{th},j}$ is given by [7, 8][16]

$$P_{\text{th},j} = \frac{c\omega_{m,j}^2 LM_j}{4Q_1 Q_{m,j} |B_j|^2} \left(1 + \frac{\Delta\omega_j^2}{(\gamma_1 + \gamma_{m,j})^2} \right), \quad (2)$$

where c is the speed of light, $\omega_{m,j}$ the mechanical mode's angular frequency, and $\Delta\omega_j = \omega_0 - \omega_1 - \omega_{m,j}$ the detuning (ω_0 : angular frequency of TEM_{00,(q)} mode; ω_1 : angular frequency of TEM_{10,(q-1)} mode). $Q_1 = \omega_1/(2\gamma_1) = \omega_1 L\mathcal{F}/(\pi c)$ and $Q_{m,j} = \omega_{m,j}/(2\gamma_{m,j})$ are the Q factors of the TEM_{10,(q-1)} and the mechanical mode, respectively (γ_1 and \mathcal{F} are the amplitude decay constant and finesse of the TEM_{10,(q-1)} mode). The effective mass of the mechanical mode is $M_j = \int_V \rho(\mathbf{r}) |\mathbf{u}_j(\mathbf{r})|^2 d\mathbf{r}$, where \mathbf{u}_j is the displacement of the mechanical mode function, ρ the mirror density, and V the mirror volume. The overlap of the mechanical and optical modes over the mirror surface S is

$$B_j = \int_S u_{z,j}(\mathbf{r}_\perp) F_0(\mathbf{r}_\perp) F_1^*(\mathbf{r}_\perp) d\mathbf{r}_\perp, \quad (3)$$

where $u_{z,j}$ is the z component (pointing along the cavity axis) of \mathbf{u}_j . The optical mode functions of the TEM_{00,(q)} and TEM_{10,(q-1)} modes, F_0 and F_1 respectively, are normalized so that $\int |F(\mathbf{r}_\perp)|^2 d\mathbf{r}_\perp = 1$.

The frequency spacing between the TEM_{00,(q)} and TEM_{10,(q-1)} modes in our near-concentric cavity is determined by the cavity geometry,

$$\Delta\nu_{01} = \frac{\omega_0 - \omega_1}{2\pi} = \frac{c \cos^{-1} \left(\frac{L-R}{R} \right)}{2\pi L} \approx \frac{c\sqrt{d}}{2\sqrt{2}\pi R^{3/2}} \quad (4)$$

where $d = 2R - L$ is the distance to concentricity, which we tune between 0.5 μm –120 μm . The mode waist W_0 and mode numerical aperture NA are related to d by $W_0 = \sqrt{\lambda L/2\pi(d/L)^{1/2}}$ and $\text{NA} = \sqrt{2\lambda/\pi L(d/L)^{1/2}}$. The front surfaces of our mirrors typically show a small astigmatism ($\Delta R \sim 1 \mu\text{m}$), which splits the otherwise degenerate TEM_{10,(q-1)} and TEM_{01,(q-1)} mode frequencies by $\gtrsim \gamma_1/(2\pi)$ (Fig. 1 (b)). PI only involves one of these

modes at a time (Appendix A), which we refer to without loss of generality as TEM_{10,(q-1)}.

Calculating the power threshold (Eq. (2)) requires knowledge of the mechanical modes involved in PI. Our approach parallels that used to describe modes in the bulk acoustic wave resonators of [17, 18], but is simplified by the fact that our ULE mirrors are isotropic. Mechanical modes can often be well described as surface waves, mostly-transverse waves in the bulk, or mostly-longitudinal waves in the bulk, with the latter describing the modes observed here. The displacement \mathbf{u} of longitudinal waves can be written in terms of a scalar potential Φ as $\mathbf{u} = \nabla\Phi$ [19], where Φ satisfies the wave equation

$$c_L^2 \nabla^2 \Phi - \ddot{\Phi} = 0 \quad (5)$$

and appropriate boundary conditions. Here, c_L is the longitudinal wave velocity (5740 m/s for ULE).

The modes must overlap well with the optical TEM_{00,(q)} and TEM_{10,(q-1)} modes (which have transverse length scales of mm), but at several MHz frequencies the wavelengths of the longitudinal modes will be $\lesssim 500 \mu\text{m}$. This justifies a paraxial approximation for the mechanical mode functions [20, 21]. Formally, we assume a set of solutions to Eq. (5) of the form $\Phi_j = U_j(x, y, z) e^{i(k_{m,j} z - \omega_{m,j} t)}$, where U_j is a slow-varying envelope function. Following the treatment of [22], we find the acoustic paraxial wave equation

$$\nabla_\perp^2 U_j + 2ik_{m,j} \partial_z U_j = 0 \quad (6)$$

with the constraint $k_{m,j} = \pm\omega_{m,j}/c_L$.

The transverse boundary conditions can be satisfied by HG modes (with transverse indices m, n and longitudinal index p), which are solutions to Eq. (6) with negligible extent at the edges of the mirror. Non-Gaussian, delocalized solutions also exist. However, only the HG modes are responsible for the observed PI, as they have higher overlap $|B_j^2|/M_j$ with the optical modes, and likely have a higher $Q_{m,j}$ since their amplitude is negligible at the mirror's mounting points (hatched elements in Fig. 1 (a); contacting mirror at radius $r > 11.6 \text{ mm}$). The mirror's front and back surfaces have stress-free boundary conditions [23]. To leading order in the paraxial parameter [22], we can compute the stress tensor components on the mirror axis ($\sigma_{xz}, \sigma_{yz}, \sigma_{zz}$) $\approx (0, 0, -k_{m,j}^2 c_L^2 \rho \Phi_j)$ from the stress-strain relation for a linear, isotropic, elastic solid. The off-axis, normal stress components on the spherical mirror surfaces will approximately take the same form, provided the wavefront curvature of the HG modes matches the curvature of the surfaces. This gives the approximate boundary condition $\Phi_j = 0$ (i.e., $u_{z,j}$ has an antinode) on the mirror's front and back surfaces. The boundary conditions for Φ_j are identical to those of an optical cavity, and the mechanical HG mode profiles therefore have the same form as the optical TEM mode profiles, albeit with different beam parameters. Explicit

forms for the mode properties, including profile functions, frequencies, and overlap integrals, are provided in the Supplemental Material.

Specifically, in our optical cavity each mirror (Fig. 1 (a)) behaves as a near-planar acoustic cavity with a nominal free spectral range of $\text{FSR}_m = (530 \pm 10)$ kHz, transverse mode spacing of $\text{TMS}_m = (46 \pm 1)$ kHz, and mode frequencies of $\omega_{m,j}/(2\pi) = p\text{FSR}_m + (m + n + 1)\text{TMS}_m$. The mirror geometry, chosen to be aplanatic to minimize optical aberrations [24], fixes the mechanical mode waist position and Rayleigh range (Fig. 1 (a)). Consequently, the mechanical mode radius $W_{m,j}(z)$ scales as $1/\sqrt{\omega_{m,j}}$. Likewise, the optical mode radius $W(z_S) \approx \lambda L/(2\pi W_0)$ at the mirror front surface scales as $1/\sqrt{\Delta\nu_{01}}$. For (nearly-)resonant modes, i.e., $\omega_{m,j}/(2\pi) \approx \Delta\nu_{01}$, all the mode profile dimensions in Eq. (3) hence scale as $1/\sqrt{\omega_{m,j}}$ (Fig. 1 (c)). If the optical and mechanical modes are centered and aligned (sharing origin and principal axes orientation, respectively), $|B_j^2|/M_j$ scales as $\omega_{m,j}$ with a mode-specific prefactor. In this case, only odd m and even n modes can overlap with the beating $\text{TEM}_{00,(q)}$ and $\text{TEM}_{10,(q-1)}$ modes, with the $(m = 1, n = 0)$ modes having the strongest overlap. This selection rule vanishes if the optical cavity is not perfectly centered (or aligned) on the mirrors. Fig. 1 (a) shows a particular mechanical mode at $\omega_{m,j}/(2\pi) = 5.4$ MHz and the optical beatnote $F_0 F_1^*$ it interacts with.

Experimental scheme.—During PI, the optical cavity oscillates in both the $\text{TEM}_{00,(q)}$ and $\text{TEM}_{10,(q-1)}$ modes. We directly observed their beatnote by detecting the RF power spectrum of the cavity transmission with a photodetector (Fig. 1 (b); an aperture at the detector ensures spatial overlap between the modes). The beatnote frequency defines the PI frequency f_{PI} (see peak in orange spectrum in Fig. 1 (b)). Because the inverse decay time of the mechanical modes ($\gamma_{m,j} < 3000 \text{ s}^{-1}$) is much smaller than that of the $\text{TEM}_{10,(q-1)}$ mode ($\gamma_1 \geq 1.5 \times 10^5 \text{ s}^{-1}$), f_{PI} corresponds to the frequency of the oscillating mechanical mode (with index j), $\omega_{m,j}/(2\pi)$ (Appendix A). Using an acousto-optic modulator (AOM; $< 2 \mu\text{s}$ rise time), we varied the circulating power $P_{\text{circ},0}$ between above (transiently) and below the power threshold $P_{\text{th},j}$ and observed the exponential rise and decay of the beatnote (Fig. 2 (a)). By repeating this for multiple values of $P_{\text{circ},0} < P_{\text{th},j}$ and using Eq. (1), we determined $P_{\text{th},j}$ and the mechanical Q factor $Q_{m,j}$ (“step-down measurement”, Fig. 2 (b)). We selected different mechanical modes by varying the optical transverse mode spacing $\Delta\nu_{01}$ (by adjusting the distance to concentricity d), and then linearly ramping up the circulating power until we observed PI. However, because of thermal expansion of the mirrors, we could not independently control the detuning $\Delta\omega_j = 2\pi\Delta\nu_{01} - \omega_{m,j}$, and instead observed that $\Delta\nu_{01} \approx f_{\text{PI}}$, i.e., $\Delta\omega_j \approx 0$, at the onset of PI (Appendix B). This thermal expansion is visible as a shift of the higher-order modes with circulating power in

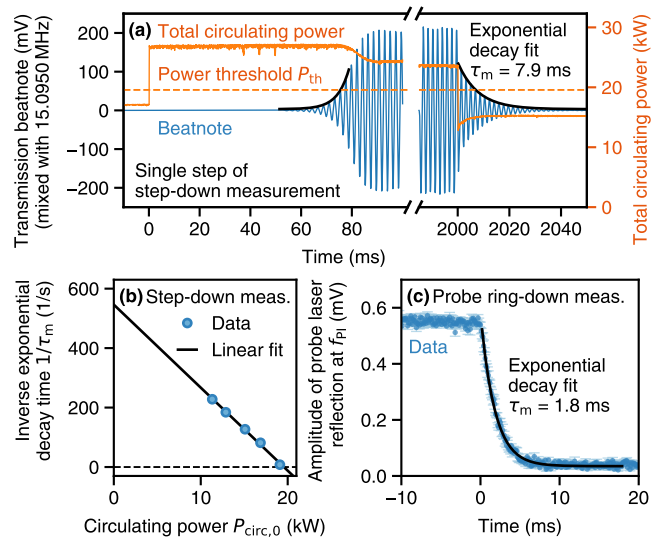


FIG. 2. (a) A single step of a step-down measurement, where the total circulating power (power $P_{\text{circ},0}$ in the $\text{TEM}_{00,(q)}$ mode plus power in $\text{TEM}_{10,(q-1)}$ mode, orange line) is first increased above the power threshold P_{th} (dashed orange line) and then reduced below it. The cavity transmission shows a beatnote, here at 15.1 MHz and mixed-down for visibility (blue line), with exponentially rising and falling envelope when the power is varied. A fit to the latter gives the mechanical mode’s exponential decay time τ_m at the final circulating power $P_{\text{circ},0}$. (b) A linear fit (black line) to the inverse decay times $1/\tau_m$ (blue circles) at powers $P_{\text{circ},0}$ gives the extrapolated power threshold P_{th} and τ_m at zero power (Eq. (1)). (c) Probe ring-down measurement, where the total circulating power (not shown) is reduced from above the power threshold P_{th} to zero (at time 0 ms). The amplitude (blue circles) of the probe laser’s reflection off the cavity at frequency f_{PI} , proportional to the amplitude of mirror vibrations, decays exponentially. A fit (black line) gives τ_m . Data are average of 7 repetitions; error bars show 1σ uncertainty.

Fig. 1 (b).

We also directly observed the mirror vibrations using a probe laser (852 nm or 948 nm wavelength) coupled into the optical cavity. Because of the low reflectance of the cavity mirrors at these wavelengths (20%–32%) and the cavity’s near-degenerate mode structure, the cavity’s spatial selectivity is low, allowing us to probe different positions (x, y) on the mirror front surface. We stabilized the probe laser to the side of the cavity fringe, and measured the local cavity length change at f_{PI} from the modulation of the reflected light. Since we expect only one mirror to vibrate at a time (Appendix A), this gives the vibration amplitude at (x, y) . By using the AOM to block the 1064-nm light, we independently inferred $Q_{m,j}$ from the exponential decay of the vibration amplitude (“probe ring-down measurement”, Fig. 2 (c)).

Observation of parametric instability.—Using this approach, we measured the power threshold P_{th} and mechanical Q factor Q_m of different mechanical modes.

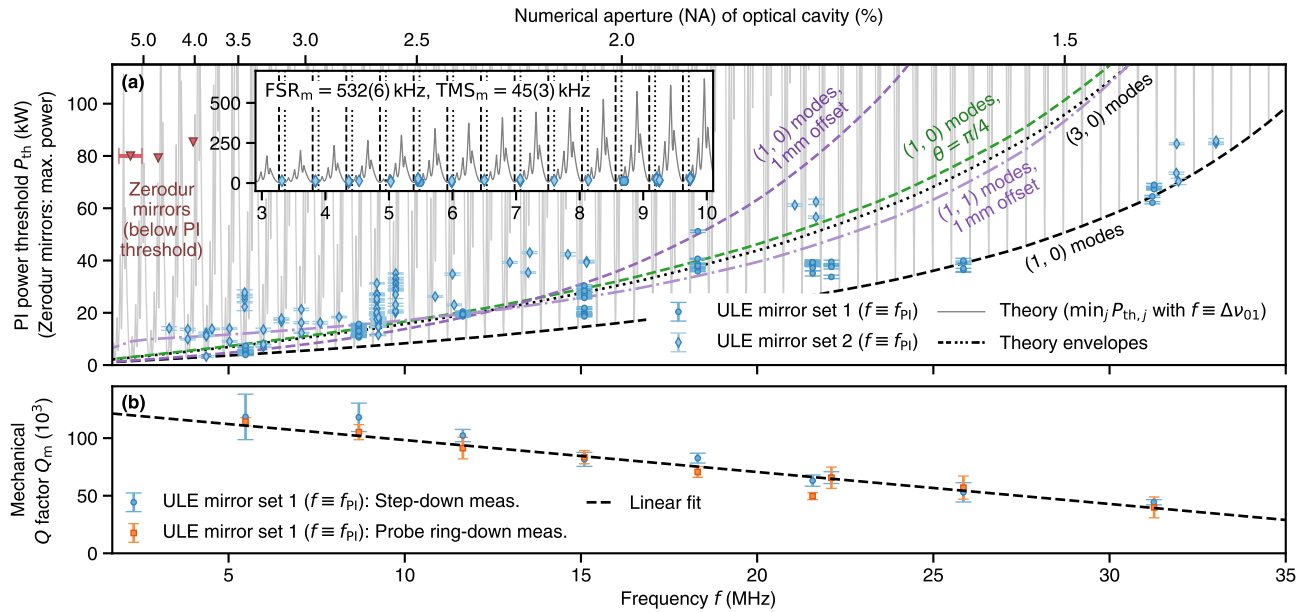


FIG. 3. (a) Measured and calculated power thresholds P_{th} of the parametric instability at frequency f . Experimental data, for which f is the observed PI oscillation frequency f_{PI} , are shown for two different sets of ULE cavity mirrors (blue circles and diamonds). The calculated $\min_j P_{th,j}$ for $f \equiv \Delta\nu_{01}$ is shown as gray solid line (assuming the optical modes are centered on the mirrors). Envelopes of $\min_j P_{th,j}$ on resonance with (1, 0) mechanical modes ($\Delta\nu_{01} = \omega_{m,j}/(2\pi)$) are shown for the optical modes centered (dashed black line; dotted black line shows (3, 0) mechanical mode), radially offset by 1 mm (dashed purple line), or rotated by $\pi/4$ (dashed green line). For the offset case, the result with the (1, 1) mechanical mode on-resonance is also shown (dash-dotted purple line). Red triangles show the maximum circulating power demonstrated with Zerodur mirrors. PI was sporadically observed at higher powers, but not characterized (see text). Finesse is set to $\mathcal{F} = 28,000$; data from mirror set 2 ($\mathcal{F} = 32,000$) were scaled accordingly. The upper axis shows the optical cavity NA for $f = \Delta\nu_{01}$. Inset: $\min_j P_{th,j}$ with experimental P_{th} , showing P_{th} clustering near the lower envelope; dashed and dotted lines mark (1, 0) and (3, 0) mechanical mode frequencies, respectively. Error bars show 1σ statistical uncertainty; 3% power calibration uncertainty not included. (b) Mechanical Q factors $Q_{m,j}$ (for mirror set 1 only) from step-down (blue circles) and probe ring-down (orange squares) measurements. Error bars show weighted standard deviation over data for step-down measurements and combined statistical and systematic 1σ uncertainty for probe ring-down measurements.

Fig. 3(a) shows P_{th} for two ULE cavity mirror sets differing primarily in coating absorption ($\alpha = 0.1$ ppm and 0.7 ppm for sets 1 and 2, respectively; blue circles and diamonds). Overall, P_{th} ranges from 3 kW at $f_{PI} \approx 4$ MHz (4% NA) to 86 kW at $f_{PI} \approx 33$ MHz (1.4% NA). From the spacing of f_{PI} , we infer $FSR_m = (532 \pm 6)$ kHz and $TMS_m = (45 \pm 3)$ kHz, in good agreement with the values expected from the mirror geometry (inset; dashed and dotted lines mark (1, 0) and (3, 0) mechanical mode frequencies, respectively).

Fig. 3(b) shows the corresponding values of Q_m determined from the step-down (blue circles) and the 948-nm probe ring-down (orange squares) measurements, with the two measurements in good agreement. We find that Q_m decreases approximately linearly with f_{PI} in the measured range of 5.5 MHz–31 MHz, with a best fit of $Q_m(f_{PI}) = 1.26(5) \times 10^5 - 2.8(2) \times 10^{-3} f_{PI}$ (dashed line). To our knowledge, this is the first measurement of the Q factor of ULE at MHz frequencies. Because the acoustic mode is localized far from the mounting points, we estimate that mounting losses place an upper limit of

$\sim 2 \times 10^8$ on Q_m for the modes observed here. A previous measurement of ULE at kHz frequencies [25], far below our measurement range, found a frequency-independent Q factor half the value we extrapolate to this range. Our measured Q_m is approximately one order of magnitude smaller than values reported for fused silica at MHz frequencies [25, 26]. Only data from ULE mirror set 1 are used to determine Q_m , as set 2's higher absorption and resulting thermal expansion were found to introduce significant nonlinearities when extrapolating τ_m in the step-down measurement.

Using the mechanical Q factor $Q_m(f_{PI})$, free spectral range FSR_m , and transverse mode spacing TMS_m , we calculate the minimum value of the power threshold $P_{th,j}$ (Eq. (2)) over all mechanical modes, i.e., $\min_j P_{th,j}$, finding that the contributing modes have $m+n \leq 10$. The result versus optical transverse mode spacing $\Delta\nu_{01}$ is shown in Fig. 3(a) (gray solid line), assuming the optical modes are centered and aligned with the mechanical modes. As expected from the thermal expansion of the mirrors (Appendix B), the experimental values are at resonance with

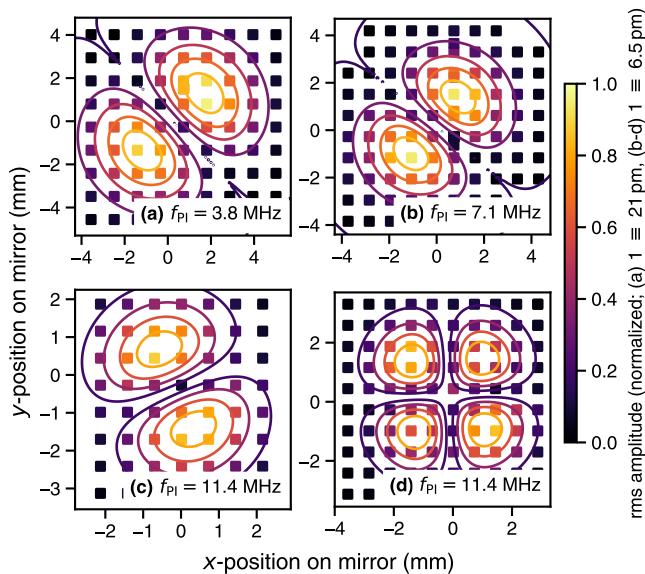


FIG. 4. Vibration amplitude profiles of the mechanical modes in the cavity mirrors excited by the parametric instability, measured with the 852-nm probe laser. The contours show fits of Hermite-Gaussian modes with indices (a–c) ($m = 1, n = 0$) and (d) (1, 1). On average, including 4 additional measurements (at $f_{\text{PI}} = 4.4$ MHz and 17.3 MHz; not shown), the fitted mechanical mode radii $W_m(z_S)$ agree within 4% with those expected from the mirror geometry (Fig. 1 (c)). Data from ULE mirror set 2.

low- (m, n) modes, near the lower limit of the calculated $P_{\text{th},j}$ (inset). The lower envelope of $\min_j P_{\text{th},j}$ occurs at resonance with (1, 0) mechanical modes (dashed black line), and agrees well with the lower envelope of the measured P_{th} values. We attribute the remaining variation in P_{th} to alignment imperfections as well as the excitation of mechanical modes other than the (1, 0) mode (other lines), as indicated by oscillation frequencies spaced by TMS_m and its multiples (inset).

Measurement of mechanical mode profiles.—The vibration amplitude profiles of four of the mechanical modes driven during PI are shown in Fig. 4, recorded by scanning the 852-nm probe laser (0.5 mm beam radius) across the cavity mirrors. These profiles are well-described by HG modes with indices (1, 0) (a–c) and (1, 1) (d), as shown by the contours of the corresponding fits, and their amplitudes match the order of magnitude expected from our theory. This agreement also holds for four additional measurements not shown here. Furthermore, we find that the principal axes of the optical modes (measured in transmission on a camera) are approximately aligned with those of the mechanical mode. We note that this measurement might be biased towards lower- (m, n) modes compared to the step-down and probe ring-down measurements, as the longer measurement time selects for modes where PI can be reliably reproduced. Overall, the fitted mechanical mode radii $W_m(z_S)$, shown in

Fig. 1 (c) (black circles), range from (1.34 ± 0.03) mm at $f_{\text{PI}} = 17.3$ MHz to (2.74 ± 0.03) mm at $f_{\text{PI}} = 3.8$ MHz and agree within 4% with those expected from the mirror geometry.

Suppression of parametric instability.—PI can be suppressed without changing the properties of the optical cavity through several approaches. These include controlling the detuning $\Delta\omega_j$ to operate far from a mechanical resonance [11, 27], decreasing the mechanical Q factor through damping [28, 29] or low- Q mirror substrates, or modifying mirror geometry to change mechanical boundary conditions (e.g., rendering the acoustic cavity unstable). The latter, combined with a high $\Delta\nu_{01} \approx 100$ MHz, likely inadvertently suppressed PI in the (20-mm long, largely enclosed) cavities used in phase-contrast electron microscopy [1, 24], as the geometry of their ULE mirrors does not support a stable acoustic cavity; in hindsight, we believe PI was observed, with a threshold consistent with our results above, in an otherwise identical test cavity with mirrors whose aplanatic geometry [24] supported bulk acoustic modes. We chose the second suppression approach, as control of the detuning is limited by thermal expansion, and the PI threshold is more challenging to predict for unstable geometries.

However, the localized nature of our mechanical modes makes damping challenging without affecting the optical modes, and attempts using an indium damper failed to provide sufficient damping while distorting the mirrors. Instead, we replaced our ULE mirrors with mirrors made from low-expansion, glass-ceramic Zerodur [30] with an otherwise identical geometry, superpolishing, and coating design. Zerodur has been reported to have a 20-fold lower Q factor than ULE at kHz frequencies [25]. With these mirrors ($\mathcal{F} = 26,000$), we achieved a maximum circulating power of 85 kW at $\Delta\nu_{01} = 4.0$ MHz (4.0% NA, 310 GW/cm² intensity; red triangles in Fig. 3 (a)). The circulating power was limited by thermal lensing due to Zerodur’s large absorption (3.4%/cm at 1064 nm), which reduced the coupling efficiency with increasing input power. Higher intensities were realized at higher NAs, reaching 380 GW/cm² at 4.6% NA before the onset of strong aberrations. Beyond NA $\approx 5\%$, the optical cavity mode was highly aberrated and the NA could no longer be accurately determined from the transverse mode spectrum; here, we imaged the cavity mode (correcting for thermal lensing by varying the circulating power) to find the peak intensity I and corresponding effective NA, $\sqrt{I\lambda^2}/(8\pi P_{\text{circ},0})$. In this regime, we achieved hour-long operation with up to (520 ± 70) GW/cm² at an effective NA of $(5.4 \pm 0.4)\%$, comparable to the highest intensities demonstrated in [1, 24], despite our 5-fold smaller distance to concentricity. We sporadically observed PI at $P_{\text{th}} \approx 80$ kW and $\Delta\nu_{01} \approx 0.9$ MHz, but were unable to directly measure the Q factor because the onset of PI was not reliably reproducible. However, the threshold suggests a Q factor of 10^3 – 10^4 , in line with the value

3.1×10^3 reported in [25] for Zerodur. It is likely that even higher intensities can be realized with ULE mirrors with a geometry that does not form a stable acoustic cavity, though care needs to be taken to minimize optical aberrations for high-NA operation.

Conclusions.—We showed that bulk mirror vibrations at MHz frequencies can limit the power and intensity of high-NA Fabry-Pérot cavities through PI. In particular, the mirrors can form stable acoustic cavities that have localized mechanical modes leading to a relatively low power threshold for the onset of PI. We measured the power thresholds, the Q factors, and the profiles of the mechanical modes, finding good agreement with the corresponding theory developed herein. The localized nature of the modes allows PI to be used as a probe of intrinsic mechanical Q factors at MHz frequencies, which we used to determine the Q factor of ULE. By externally driving the higher-order optical mode, this technique could also be used without reaching the PI threshold. Finally, we demonstrated that low- Q mirrors (here made from Zerodur) suppress PI, allowing us to reach intensities in excess of 500 GW/cm^2 in an open, free-space cavity. Notably, such intensities enable ultradeep, buffer-gas-loaded dipole traps for molecules, including for low-polarizability species like atomic and molecular hydrogen [6].

The authors thank E. S. Cooper for insightful theory discussions, J. J. Axelrod for help with the set-up of the test cavity, S. Straßer and P. Stromberger for help with developing a mirror inspection microscope, P. N. Petrov and J. T. Zhang for helpful discussions, and R. Patterson for technical advice on optical coatings. This work was supported by the Brown Science Foundation through the Brown Investigator Award (award no. 1167), the Gordon and Betty Moore Foundation (grant no. 9366), the Chan Zuckerberg Initiative (award no. 2021-234606 and 2025-367757), the Heising-Simons Foundation (grant no. 2023-4467), and the U.S. Department of Energy, Office of Science, National Quantum Information Science Research Centers, Quantum Systems Accelerator (award no. DESCL0000121). L. M. acknowledges a Feodor Lynen Fellowship from the Alexander von Humboldt Foundation. A. S. acknowledges support from the UC Berkeley Physics Department’s Graduate Student Support Fund.

-
- * These authors contributed equally to this work
- [1] C. Turnbaugh, J. J. Axelrod, S. L. Campbell, J. Y. Dioquino, P. N. Petrov, J. Remis, O. Schwartz, Z. Yu, Y. Cheng, R. M. Glaeser, and H. Mueller, High-power near-concentric Fabry–Perot cavity for phase contrast electron microscopy, *Review of Scientific Instruments* **92**, 053005 (2021).
 - [2] H. Müller, J. Jin, R. Danev, J. Spence, H. Padmore, and R. M. Glaeser, Design of an electron microscope phase plate using a focused continuous-wave laser, *New Journal of Physics* **12**, 073011 (2010).
 - [3] O. Schwartz, J. Axelrod, D. R. Tuthill, P. Haslinger, C. Ophus, R. Glaeser, and H. Müller, Near-concentric Fabry–Pérot cavity for continuous-wave laser control of electron waves, *Optics Express* **25**, 14453 (2017).
 - [4] O. Schwartz, J. J. Axelrod, S. L. Campbell, C. Turnbaugh, R. M. Glaeser, and H. Müller, Laser phase plate for transmission electron microscopy, *Nature Methods* **16**, 1016 (2019).
 - [5] J. J. Axelrod, S. L. Campbell, O. Schwartz, C. Turnbaugh, R. M. Glaeser, and H. Müller, Observation of the relativistic reversal of the ponderomotive potential, *Physical Review Letters* **124**, 174801 (2020).
 - [6] A. Singh, L. Maisenbacher, Z. Lin, J. J. Axelrod, C. D. Panda, and H. Müller, Dynamics of a buffer-gas-loaded, deep optical trap for molecules, *Physical Review Research* **5**, 033008 (2023).
 - [7] V. B. Braginsky, S. E. Strigin, and S. P. Vyatchanin, Parametric oscillatory instability in Fabry–Perot interferometer, *Physics Letters A* **287**, 331 (2001).
 - [8] M. Evans, L. Barsotti, and P. Fritschel, A general approach to optomechanical parametric instabilities, *Physics Letters A* **374**, 665 (2010).
 - [9] H. Rokhsari, T. J. Kippenberg, T. Carmon, and K. J. Vahala, Radiation-pressure-driven micro-mechanical oscillator, *Optics Express* **13**, 5293 (2005).
 - [10] T. J. Kippenberg, H. Rokhsari, T. Carmon, A. Scherer, and K. J. Vahala, Analysis of radiation-pressure induced mechanical oscillation of an optical microcavity, *Physical Review Letters* **95**, 033901 (2005).
 - [11] M. Evans, S. Gras, P. Fritschel, J. Miller, L. Barsotti, D. Martynov, A. Brooks, D. Coyne, R. Abbott, R. X. Adhikari, K. Arai, R. Bork, B. Kells, J. Rollins, N. Smith-Lefebvre, G. Vajente, H. Yamamoto, C. Adams, S. Aston, J. Betzweiser, V. Frolov, A. Mullahey, A. Pele, J. Romie, M. Thomas, K. Thorne, S. Dwyer, K. Izumi, K. Kawabe, D. Sigg, R. Derosa, A. Effler, K. Kokeyama, S. Ballmer, T. J. Massinger, A. Staley, M. Heinze, C. Mueller, H. Grote, R. Ward, E. King, D. Blair, L. Ju, and C. Zhao, Observation of parametric instability in Advanced LIGO, *Physical Review Letters* **114**, 161102 (2015).
 - [12] X. Chen, C. Zhao, S. Danilishin, L. Ju, D. Blair, H. Wang, S. P. Vyatchanin, C. Molinelli, A. Kuhn, S. Gras, T. Briant, P.-F. Cohadon, A. Heidmann, I. Roch-Jeune, R. Flaminio, C. Michel, and L. Pinard, Observation of three-mode parametric instability, *Physical Review A* **91**, 033832 (2015).
 - [13] P. Kharel, G. I. Harris, E. A. Kittlaus, W. H. Renninger, N. T. Otterstrom, J. G. E. Harris, and P. T. Rakich, High-frequency cavity optomechanics using bulk acoustic phonons, *Science Advances* **5**, eaav0582 (2019).
 - [14] V. Sudhir, *Quantum Limits on Measurement and Control of a Mechanical Oscillator*, Ph.D. thesis, EPFL, Lausanne (2016).
 - [15] Corning ULE 7972, 0.7%/cm absorption at 1064 nm.
 - [16] In [7], the denominator in the parentheses in Eq. (2) is $(\gamma_1 - \gamma_{m,j})^2$, which we have corrected to $(\gamma_1 + \gamma_{m,j})^2$ (Appendix A). In the usual limit $\gamma_{m,j} \ll \gamma_1$, the results are equivalent.
 - [17] P. Kharel, Y. Chu, M. Power, W. H. Renninger, R. J. Schoelkopf, and P. T. Rakich, Ultra-high-Q phononic resonators on-chip at cryogenic temperatures, *APL Photonics* **3**, 066101 (2018).
 - [18] W. H. Renninger, P. Kharel, R. O. Behunin, and P. T. Rakich, Bulk crystalline optomechanics, *Nature Physics* **14**, 601 (2018).
 - [19] T. Lay and T. C. Wallace, *Modern Global Seismology*, International Geophysics Series No. 58 (Academic Press, San Diego, 1995).
 - [20] B. D. Cook and W. J. Arnoult, III, Gaussian–Laguerre/Hermite formulation for the nearfield of an ultrasonic transducer, *The Journal of the Acoustical Society of America* **59**, 9 (1976).
 - [21] B. P. Newberry and R. B. Thompson, A paraxial theory for the propagation of ultrasonic beams in anisotropic solids, *The Journal of the Acoustical Society of America* **85**, 2290 (1989).
 - [22] M. Lax, W. H. Louisell, and W. B. McKnight, From Maxwell to paraxial wave optics, *Physical Review A* **11**, 1365 (1975).
 - [23] S. N. Rasband, Resonant vibrations of free cylinders and disks, *The Journal of the Acoustical Society of America* **57**, 899 (1975).
 - [24] J. J. Axelrod, *A Laser Phase Plate for Transmission Electron Microscopy*, Ph.D. thesis, University of California, Berkeley (2024), arXiv:2403.10670.
 - [25] K. Numata, A. Kemery, and J. Camp, Thermal-noise limit in the frequency stabilization of lasers with rigid cavities, *Physical Review Letters* **93**, 250602 (2004).
 - [26] W. J. Startin, M. A. Beilby, and P. R. Saulson, Mechanical quality factors of fused silica resonators, *Review of Scientific Instruments* **69**, 3681 (1998).
 - [27] T. Hardwick, V. J. Hamedan, C. Blair, A. C. Green, and D. Vander-Hyde, Demonstration of dynamic thermal compensation for parametric instability suppression in Advanced LIGO, *Classical and Quantum Gravity* **37**, 205021 (2020).
 - [28] C. Blair, S. Gras, R. Abbott, S. Aston, J. Betzwieser, D. Blair, R. DeRosa, M. Evans, V. Frolov, P. Fritschel, H. Grote, T. Hardwick, J. Liu, M. Lormand, J. Miller, A. Mullahey, B. O’Reilly, C. Zhao, LSC Instrument Authors, B. P. Abbott, T. D. Abbott, C. Adams, R. X. Adhikari, S. B. Anderson, A. Ananyeva, S. Appert, K. Arai, S. W. Ballmer, D. Barker, B. Barr, L. Barsotti, J. Bartlett, I. Bartos, J. C. Batch, A. S. Bell, G. Billingsley, J. Birch, S. Biscans, C. Biwer, R. Bork, A. F. Brooks, G. Ciani, F. Clara, S. T. Countryman, M. J. Cowart, D. C. Coyne, A. Cumming, L. Cunningham, K. Danzmann, C. F. Da Silva Costa, E. J. Daw, D. DeBra, R. DeSalvo, K. L. Dooley, S. Doravari, J. C. Driggers, S. E. Dwyer, A. Effler, T. Etzel, T. M. Evans, M. Factourovich, H. Fair, A. Fernández Galiana, R. P. Fisher, P. Fulda, M. Fyffe, J. A. Giaime, K. D. Gardina, E. Goetz, R. Goetz, C. Gray, K. E. Gushwa, E. K. Gustafson, R. Gustafson, E. D. Hall, G. Hammond,

J. Hanks, J. Hanson, G. M. Harry, M. C. Heintze, A. W. Heptonstall, J. Hough, K. Izumi, R. Jones, S. Kandhasamy, S. Karki, M. Kasprzack, S. Kaufer, K. Kawabe, N. Kijbunchoo, E. J. King, P. J. King, J. S. Kissel, W. Z. Korth, G. Kuehn, M. Landry, B. Lantz, N. A. Lockerbie, A. P. Lundgren, M. MacInnis, D. M. Macleod, S. Márka, Z. Márka, A. S. Markosyan, E. Maros, I. W. Martin, D. V. Martynov, K. Mason, T. J. Massinger, F. Matichard, N. Mavalvala, R. McCarthy, D. E. McClelland, S. McCormick, G. McIntyre, J. McIver, G. Mendell, E. L. Merilh, P. M. Meyers, R. Mittleman, G. Moreno, G. Mueller, J. Munch, L. K. Nuttall, J. Oberling, P. Oppermann, R. J. Oram, D. J. Ottaway, H. Overmier, J. R. Palamos, H. R. Paris, W. Parker, A. Pele, S. Penn, M. Phelps, V. Pierro, I. Pinto, M. Principe, L. G. Prokhorov, O. Puncken, V. Quetschke, E. A. Quintero, F. J. Raab, H. Radkins, P. Raffai, S. Reid, D. H. Reitze, N. A. Robertson, J. G. Rollins, V. J. Roma, J. H. Romie, S. Rowan, K. Ryan, T. Sadecki, E. J. Sanchez, V. Sandberg, R. L. Savage, R. M. S. Schofield, D. Sellers, D. A. Shaddock, T. J. Shaffer, B. Shapiro, P. Shawhan, D. H. Shoemaker, D. Sigg, B. J. J. Slagmolen, B. Smith, J. R. Smith, B. Sorazu, A. Staley, K. A. Strain, D. B. Tanner, R. Taylor, M. Thomas, P. Thomas, K. A. Thorne, E. Thrane, C. I. Torrie, G. Traylor, G. Vajente, G. Valdes, A. A. van Veggel, A. Vecchio, P. J. Veitch, K. Venkateswara, T. Vo, C. Vorvick, M. Walker, R. L. Ward, J. Warner, B. Weaver, R. Weiss, P. Weßels, B. Willke, C. C. Wipf, J. Worden, G. Wu, H. Yamamoto, C. C. Yancey, H. Yu, H. Yu, L. Zhang, M. E. Zucker, and J. Zweizig, First demonstration of electrostatic damping of parametric instability at Advanced LIGO, *Physical Review Letters* **118**, 151102 (2017).

- [29] S. Biscans, S. Gras, C. D. Blair, J. Driggers, M. Evans, P. Fritschel, T. Hardwick, and G. Mansell, Suppressing parametric instabilities in LIGO using low-noise acoustic mode dampers, *Physical Review D* **100**, 122003 (2019).
- [30] Schott Zerodur Expansion Class 0 Special.
- [31] Matthew J. Aburn, sdeint0.3.0 (2022).

APPENDIX A: DETAILS OF THE PI THRESHOLD AND TIME DYNAMICS

Using the same methods as [7], we can derive dynamical equations of motion for the slow-varying field amplitudes D_0 , D_1 , and X of the $\text{TEM}_{00,(q)}$, $\text{TEM}_{10,(q-1)}$ and mechanical modes (we here omit the mode index j), respectively, in the rotating wave approximation:

$$\dot{D}_0 + \gamma_0(D_0 - D_{0,\text{sp}}) = -i\omega_1 B^* X D_1 e^{i\Delta\omega t}/L, \quad (7a)$$

$$\dot{D}_1 + \gamma_1 D_1 = -i\omega_0 B X^* D_0 e^{-i\Delta\omega t}/L, \quad (7b)$$

$$\dot{X} + \gamma_m X = \frac{-i\epsilon_0\omega_0\omega_1}{2M\omega_m} B D_0 D_1^* e^{-i\Delta\omega t} + \hat{f}_n, \quad (7c)$$

where we have added a drive field ('setpoint') $D_{0,\text{sp}}$ and a stochastic noise term \hat{f}_n to the differential equations of [7] (γ_0 : amplitude decay constant of $\text{TEM}_{00,(q)}$ mode). The exact form of \hat{f}_n is unimportant for the overall dynamics, as its sole purpose is to provide an initial excitation of the mechanical mode. We choose a Langevin noise term $\hat{f}_n = \sqrt{\gamma_m k_B T / (2M)} R(t) e^{i\omega_m t}$, with $R(t)$ a delta-correlated Gaussian white noise process (k_B : Boltzmann constant). With this definition of slow-varying amplitudes, the circulating electric field is

$$F_{\text{circ}}(\mathbf{r}, t) = \sum_{a=0,1} \text{Re} \left(i\omega_a D_a(t) U_a(\mathbf{r}) e^{i(k_a z - \omega_a t)} \right), \quad (8)$$

with the envelopes U_a defined in the Supplemental Material. The circulating power in an optical cavity mode indexed by $a \in \{0, 1\}$ is $P_{\text{circ},a} = \epsilon_0 c \omega_a^2 |D_a(t)|^2 / 2$, while the stored energy in the cavity mode is $E_a = 2LP_{\text{circ},a}/c$, and the stored energy in the mechanical mode is $E_m = 2M\omega_m^2 |X|^2$.

Eqs. (7a-7c) apply to the here-relevant case, where the optomechanical coupling mechanism is radiation pressure acting on the mirror surface. Electrostrictive optomechanical coupling in the bulk of a mechanical resonator has also been observed to induce PI [13]. However, in our optical cavity, the region of highest electric field is localized within a few layers of the mirror coating, where the acoustic mode has nearly zero strain due to its boundary condition. The electrostrictive interaction is thus orders of magnitude weaker than radiation pressure, and can be ignored. Thermoelastic optomechanical coupling, as seen in [14], is similarly orders of magnitude too small to consider in this work, as the PI frequencies of several MHz are much faster than the thermal diffusion timescales in the coating (\sim kHz), which itself has a small coefficient of thermal expansion ($\sim 10^{-6} \text{ K}^{-1}$).

The system of nonlinear, stochastic differential equations Eqs. (7a-7c) is integrated numerically [31], and the results are shown in Fig. 5. When the $\text{TEM}_{00,(q)}$ power is driven above the threshold, after a short time, its power drops, while the power circulating in the $\text{TEM}_{10,(q-1)}$ and mechanical modes grows. $P_{\text{circ},0}$ settles to the threshold value given in Eq. (2), where it remains constant. The

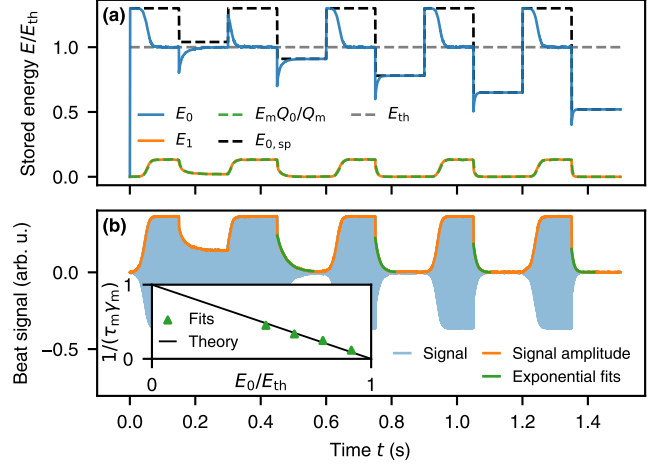


FIG. 5. Numerical integration of Eqs. (7a-7c). (a) Stored energy in the $\text{TEM}_{00,(q)}$, $\text{TEM}_{10,(q-1)}$ and mechanical modes (E_0 , E_1 and E_m , respectively), relative to the PI threshold energy $E_{\text{th}} = 2LP_{\text{th}}/c$. Due to the drastically different scales of stored mechanical and optical energy, we show E_m multiplied by Q_0/Q_m , which has the same (average) magnitude as E_1 . E_0 initially follows the drive value $E_{0,\text{sp}} \propto |D_{0,\text{sp}}|^2$ (black dashed line), before a spontaneous thermal fluctuation from \hat{f}_n initiates oscillation through PI, and E_0 drops to the threshold value (gray dashed line). The setpoint energy is stepped down in the same manner as in the experiment (Fig. 2). In the simulation, $Q_0 = 7 \times 10^5 Q_m$, $\gamma_1 = \gamma_0$, $\gamma_m = \gamma_0/400$ and $\Delta\omega = -\gamma_0$, which are typical values. (b) The beat signal $D_0 D_1^*$ (in the rotating frame) is shown in blue oscillating at $\sigma \approx \Delta\omega$, and the amplitude $|D_0 D_1^*|$ in orange. At each step-down of the drive field to a value below the threshold, an exponential decay is fit to the signal, shown in green. The inset shows the time constants of the fits against the circulating power after the step-down, in good agreement with the theoretical prediction of Eq. (1).

dynamics in the simulation qualitatively agree with the dynamics in Fig. 2, though the specifics depend on the mode being measured.

To derive the power threshold, we assume the D_0 field attains a steady-state value, neglect the small noise term \hat{f}_n , and look at the reduced system of differential equations for D_1 and X , which is now linear. Introducing $\xi = X e^{i\Delta\omega t}$, we find a time-independent linear system in D_1 and ξ^* , whose characteristic equation is

$$(-\gamma_1 - \lambda)(-\gamma_m - i\Delta\omega - \lambda) - A = 0, \quad (9)$$

where $A = \epsilon_0 \omega_0^2 \omega_1 |B|^2 |D_0|^2 / (2M\omega_m L)$. The power threshold is given by the value for D_0 above which the eigenvalue λ_+ has a positive real part, where

$$\lambda_+ = \frac{-\gamma_1 - \gamma_m - i\Delta\omega + \sqrt{(\gamma_1 - \gamma_m - i\Delta\omega)^2 + 4A}}{2}. \quad (10)$$

At this point, [7] makes an approximation in smallness of A to show the existence of the power threshold,

and computes it within this approximation. However, knowing a solution exists, we can write it down exactly by asserting that at the power threshold, one eigenvalue becomes $\lambda = 0 + i\sigma$, where $\sigma \in \mathbb{R}$. By equating the imaginary parts of Eq. (9), we find

$$\sigma = \frac{-\gamma_1}{\gamma_1 + \gamma_m} \Delta\omega \approx -\Delta\omega. \quad (11)$$

Thus, during PI, $D_1 \sim e^{i\sigma t}$, which tells us the oscillation frequency of the PI signal from

$$D_0 D_1^* e^{-i(\omega_0 - \omega_1)t} \sim e^{-i(\omega_0 - \omega_1 + \sigma)t} \approx e^{-i\omega_m t}, \quad (12)$$

i.e., $f_{\text{PI}} \approx \omega_m/(2\pi)$, regardless of $\Delta\omega$.

Meanwhile, by equating the real parts of Eq. (9), we can compute the threshold

$$A_{\text{th}} = \gamma_1 \gamma_m \left(1 + \frac{\Delta\omega^2}{(\gamma_1 + \gamma_m)^2} \right), \quad (13)$$

which rearranges to Eq. (2). Note that since $\gamma_m \ll \gamma_1$, we have $A \ll \gamma_1^2 + \Delta\omega^2$ for powers around or below the power threshold, which justifies the approximation at the end of the Appendix of [7]. Within this approximation, we can use Eq. (10) to write the mechanical mode exponential decay time $\tau_m = -1/\text{Re}(\lambda_+)$ in the form of Eq. (1).

This work assumes each PI only involves one mechanical mode at a time. While in general, many mechanical modes can be coherently driven by the beating optical fields, in practice the extremely narrow mechanical mode linewidths lead to only one mode being excited in any particular instance of PI. Multiple distinct PIs can be driven simultaneously, however, if $P_{\text{circ},0}$ exceeds the threshold of PI for two different mechanical modes, which can happen in the transitory period before onset of PI above its power threshold.

APPENDIX B: THERMAL EFFECTS

With the high circulating powers used in our experiments, even small amounts of absorption in the mirror coating can lead to significant thermal effects. In particular, the thermal expansion of the mirrors increases the distance to concentricity $d = 2R - L$ and hence changes the optical mode spacing (Eq. (4)). Despite using mirrors made from ULE, we find that the optical mode spacing can shift on the order of several optical linewidths as the circulating power is increased to the PI threshold. This can be approximately modeled by keeping the differential equations for the optical and mechanical fields (Eq. (7)), and allowing $\Delta\omega(t)$ to be a dynamical variable. $\Delta\omega(t)$ will exponentially approach, with a timescale α , a set value which depends on the circulating power:

$$\dot{(\Delta\omega)} = \alpha(\Delta\omega_{\text{init}} + \beta P_{\text{circ},0} - \Delta\omega(t)), \quad (14)$$

where $\Delta\omega_{\text{init}}$ is the initial value of $\Delta\omega(t)$ at zero circulating power $P_{\text{circ},0}$. Power in the $\text{TEM}_{10,(q-1)}$ is ignored, as it is usually significantly lower than $P_{\text{circ},0}$, and is spread over a larger area on the mirror. From empirical observations, the time constant α is of order 1 s^{-1} . Since the timescale of the dynamics of the optical and mechanical fields is significantly faster than $1/\alpha$, at any given $\Delta\omega(t)$ a power threshold is defined by

$$P_{\text{th}}(t) = P_{\text{th,res}} \left(1 + \frac{\Delta\omega^2(t)}{(\gamma_1 + \gamma_m)^2} \right). \quad (15)$$

where $P_{\text{th,res}} = c\omega_m^2 LM/(4Q_1 Q_m |B|^2)$.

Now suppose the $\text{TEM}_{00,(q)}$ mode is driven well above its power threshold at some $\Delta\omega(t)$. $P_{\text{circ},0}$ is pinned at $P_{\text{th}}(t)$, which we can insert into Eq. (14) to find an equation for the slow-timescale dynamics,

$$\frac{1}{\alpha} \frac{d\Delta\omega}{dt} = \frac{\beta P_{\text{th,res}} \Delta\omega^2(t)}{(\gamma_1 + \gamma_m)^2} - \Delta\omega(t) + (\Delta\omega_{\text{init}} + \beta P_{\text{th,res}}). \quad (16)$$

For a stable equilibrium of Eq. (16) to exist, the discriminant $\Delta_{\text{therm}} = 1 - 4\beta P_{\text{th,res}}(\Delta\omega_{\text{init}} + \beta P_{\text{th,res}})/(\gamma_1 + \gamma_m)^2$ must be positive. In this case, the stable equilibrium is

$$\Delta\omega_{\text{stable eq}} = \frac{1 - \sqrt{\Delta_{\text{therm}}}}{2\beta P_{\text{th,res}}/(\gamma_1 + \gamma_m)^2} \leq \frac{(\gamma_1 + \gamma_m)^2}{2\beta P_{\text{th,res}}}. \quad (17)$$

It is therefore impossible to drive PI at a detuning above $\Delta\omega = (\gamma_1 + \gamma_m)^2/2\beta P_{\text{th,res}} \ll \gamma_1/2$. If the cavity geometry is adjusted so that $\Delta\omega$ exceeds this limit, the cavity circulating power can be increased until the optical mode spacing shifts near-resonant to the next-higher mechanical mode free spectral range, where it will begin oscillating in a new mode.

We empirically find β to have an approximately linear frequency dependence, with $\beta \sim \gamma_1/P_{\text{th,res}}$ at $f_{\text{PI}} \sim 5\text{ MHz}$ and $\beta \sim 70\gamma_1/P_{\text{th,res}}$ at $f_{\text{PI}} \sim 30\text{ MHz}$ in ULE mirror set 2 (Fig. 1 (b)), and approximately 7-fold lower for mirror set 1 owing to its lower coating absorption. Since β is comparable to or larger than γ_1/P_{th} , $\Delta\omega$ will respond to a power increase by ending up close to resonance to a low-threshold mechanical mode in the next free spectral range, where PI again clamps the circulating power at a threshold similar to its previous level. For this reason, the experimental values of P_{th} cluster close to the lower envelope of the calculated thresholds for low- (m,n) , and thereby low threshold, modes (Fig. 3). We note that we did not attempt to maximize the circulating power, e.g., by finding an optimal power ramping scheme, as thermal drifts would likely preclude stable long-term operation.

Supplemental Material for *Ultrahigh continuous-wave intensities in high-NA optical cavities through suppression of the parametric oscillatory instability*

EXPLICIT FORMS FOR MODE FUNCTIONS AND OVERLAP INTEGRALS

In this section, we need to be careful to distinguish between properties of the optical modes and of the mechanical modes, which both have similar forms. We will use the convention that a tilde denotes a mechanical property where it may otherwise be confused with an optical property. This is in contrast to the notation used in the main text, where the subscript ‘m’ was used to label mechanical properties, as we here need subscripts to index several other properties.

The paraxial wave equation, which may describe either optical or mechanical modes in this work, is given by

$$\nabla_{\perp}^2 U + 2ik\partial_z U = 0. \quad (\text{S1})$$

The Hermite-Gaussian modes, which are traveling-wave solutions to Eq. (S1), are parametrized by the beam waist $W^{(0)}$ and the wavenumber k and indexed by transverse indices m and n . They are

$$U_{mn}(\mathbf{r}; k, W^{(0)}, z^{(0)}) = \frac{1}{\sqrt{2^{m+n-1} m! n! \pi W(z)^2}} H_m\left(\frac{\sqrt{2}x}{W(z)}\right) H_n\left(\frac{\sqrt{2}y}{W(z)}\right) e^{-\frac{x^2+y^2}{W(z)^2}} e^{\frac{ik(x^2+y^2)}{2R(z)}} e^{-i(m+n+1)\psi(z)}, \quad (\text{S2})$$

where $W(z) = W^{(0)}\sqrt{1 + (z - z^{(0)})^2/z_R^2}$, $z_R = k(W^{(0)})^2/2$, $R(z) = (z - z^{(0)}) + z_R^2/(z - z^{(0)})$, $\psi(z) = \tan^{-1}((z - z^{(0)})/z_R)$, $H_m(x)$ is the Hermite polynomial of degree m , and $z^{(0)}$ is the position of the beam’s waist along the propagation (z) axis. These functions are normalized so that $\int U_{mn}(\mathbf{r}_{\perp}, z) U_{m'n'}^*(\mathbf{r}_{\perp}, z) d\mathbf{r}_{\perp} = \delta_{mm'}\delta_{nn'}$, where δ is the Kronecker delta.

The mechanical (scalar potential) mode functions Φ_j are indexed by j , which refers to the tuple of indices $j = (m_j, n_j, p_j)$ (m_j : x -transverse mode index; n_j : y -transverse mode index; p_j : longitudinal mode index). They are given by

$$\Phi_j(\mathbf{r}, t) = A_j \text{Re} \left[\text{Im} \left[e^{i\varphi_j} U_{m_j n_j}(\mathbf{r}; \tilde{k}_j, \tilde{W}_{0,j}) e^{i\tilde{k}_j z} \right] e^{-i\tilde{\omega}_j t} \right], \quad (\text{S3})$$

where $\tilde{W}_{0,j}$ is the mechanical mode waist and $\varphi_j = (m_j + n_j + 1)\tilde{\psi}(z_S) - \tilde{k}_j(z_S)$, with z_S the position of the mirror’s front (reflective) surface. $\tilde{\omega}_j = c_L \tilde{k}_j$ is the mechanical mode angular frequency

$$\frac{\tilde{\omega}_j}{2\pi} = \frac{c_L}{2h} \left(p_j + \frac{(m_j + n_j + 1)}{\pi} \cos^{-1} \left(\sqrt{\tilde{g}_1 \tilde{g}_2} \right) \right), \quad (\text{S4})$$

where $\tilde{g}_1 = 1 - h/R_B = 0.84$ and $\tilde{g}_2 = 1 - h/(-R) = 1.11$ are the mechanical cavity g-parameters. The amplitude A_j is an arbitrary choice of normalization that is canceled out in $|B|^2/M$: we choose the convention $A_j = \sqrt{2\pi} \tilde{W}_{0,j} / \tilde{k}_j$, which makes B dimensionless and M have dimensions of mass. The displacement amplitude u_z that appears in Eq. (3) in the main text is, at leading order in the paraxial parameter and up to appropriate factors of i ,

$$u_{z,j}(\mathbf{r}_{\perp}) = \sqrt{2\pi} \tilde{W}_{0,j} U_{m_j n_j}(x, y, z_S; \tilde{k}_j, \tilde{W}_{0,j}, \tilde{z}_0). \quad (\text{S5})$$

The mirror front surface position z_S relative to the mechanical mode waist at \tilde{z}_0 and the mechanical Rayleigh range are given by

$$z_S - \tilde{z}_0 = h - \frac{h\tilde{g}_2(1 - \tilde{g}_1)}{\tilde{g}_1 + \tilde{g}_2 - 2\tilde{g}_1\tilde{g}_2} = -5.37 \text{ mm}, \quad (\text{S6})$$

$$\tilde{z}_R = \sqrt{\frac{\tilde{g}_1\tilde{g}_2(1 - \tilde{g}_1\tilde{g}_2)h^2}{(2\tilde{g}_1\tilde{g}_2 - \tilde{g}_1 - \tilde{g}_2)^2}} = 15.48 \text{ mm}, \quad (\text{S7})$$

from which $\tilde{W}_{0,j} = \sqrt{2\tilde{z}_R/\tilde{k}_j}$ follows. The effective masses of the modes are

$$M_j = \pi \tilde{W}_{0,j}^2 h \rho. \quad (\text{S8})$$

The optical mode functions in Eq. (3) of the $\text{TEM}_{00,(q)}$ and $\text{TEM}_{10,(q-1)}$ modes are, up to appropriate factors of i ,

$$F_0(\mathbf{r}_\perp) = U_{00}(\mathbf{r}_\perp, z_S; \omega_0/c, W_0, z_0), \quad F_1(\mathbf{r}_\perp) = U_{10}(\mathbf{r}_\perp, z_S; \omega_1/c, W_0, z_0), \quad (\text{S9})$$

where W_0 is the optical mode waist and $z_S - z_0 \approx L/2$ is the position of the mirror front surface relative to the optical waist.

To compute the overlap integral B in Eq. (3) requires an integral over a curved spherical surface. However, within the paraxial approximation, we can compute the overlap integral over constant z plane defined by the center of the mirror's curved surface (the surface S), provided we ignore the wavefront curvature factor in each U_{mn} function (which is matched to the spherical surface curvature). In the general case, the principal axes of the mechanical modes may be rotated by an angle θ relative to those of the optical modes, which can in turn be offset from the mechanical mode axes by (x_c, y_c) . In this context, the overlap integrals are (up to a global phase)

$$B_j(x_c, y_c, \theta) = C_j \int_{\mathbb{R}^2} (x - x_c) H_{m_j} \left(\frac{\sqrt{2}x'}{\tilde{W}_j(z_S)} \right) H_{n_j} \left(\frac{\sqrt{2}y'}{\tilde{W}_j(z_S)} \right) \exp \left(-\frac{x^2 + y^2}{\tilde{W}_j(z_S)^2} - 2\frac{(x - x_c)^2 + (y - y_c)^2}{W(z_S)^2} \right) dx dy, \quad (\text{S10})$$

where

$$C_j = \frac{8\tilde{W}_{0,j}}{\pi W(z_S)^3 \tilde{W}_j(z_S) \sqrt{2^{(m_j+n_j)} m_j! n_j!}}. \quad (\text{S11})$$

$W(z_S)$ and $\tilde{W}_j(z_S)$ are the optical and mechanical beam radii at the mirror front surface S , respectively, and $(x', y') = (x \cos \theta + y \sin \theta, -x \sin \theta + y \cos \theta)$. This formula has a closed-form result, which can be computed using Feldheim's formulae (46) and (77) [S1] (and correcting an erroneous $(-1)^k$ which should read $(-1)^r$ in Feldheim's (77)).

$$B_j(x_c, y_c, \theta) = \sum_{l=0}^{m_j+n_j} \sqrt{\frac{l!(m_j+n_j-l)!}{m_j!n_j!}} a_{m_j n_j; l}(\theta) b_{l, m_j+n_j-l}, \quad (\text{S12})$$

where

$$a_{\mu\nu;l}(\theta) = \sum_{r=0}^l (-1)^r \binom{\nu}{r} \binom{\mu}{l-r} \sin^{\mu+2r-l}(\theta) \cos^{\nu+l-2r}(\theta), \quad (\text{S13})$$

$$b_{\mu\nu} = \frac{8\tilde{W}_{0,j} W_e^4 (1 - 2W_e^2/\tilde{W}_j(z_S)^2)^{\frac{\mu+\nu}{2}}}{W(z_S)^3 \tilde{W}_j(z_S) \sqrt{2^{\mu+\nu} \mu! \nu!}} H_\nu(A_y) \left[\frac{\mu\sqrt{2}H_{\mu-1}(A_x)}{\sqrt{\tilde{W}_j(z_S)^2 - 2W_e^2}} - \frac{x_c H_\mu(A_x)}{\tilde{W}_j(z_S)^2} \right] \exp \left(\frac{-2(x_c^2 + y_c^2)}{W(z_S)^2 + 2\tilde{W}_j(z_S)^2} \right), \quad (\text{S14})$$

and

$$W_e = \sqrt{\frac{\tilde{W}_j(z_S)^2 W(z_S)^2}{2\tilde{W}_j(z_S)^2 + W(z_S)^2}}, \quad A_x = \frac{2\sqrt{2}x_c W_e^2}{W(z_S)^2 \sqrt{\tilde{W}_j(z_S)^2 - 2W_e^2}}, \quad A_y = \frac{2\sqrt{2}y_c W_e^2}{W(z_S)^2 \sqrt{\tilde{W}_j(z_S)^2 - 2W_e^2}}. \quad (\text{S15})$$

In particular, in the case that the optical and mechanical modes are perfectly aligned ($x_c = y_c = 0$ and $\theta = 0$), we find

$$B_j(0, 0, 0) = \begin{cases} \frac{8\tilde{W}_{0,j}}{\sqrt{m_j!n_j!}} \frac{W(z_S)\tilde{W}_j(z_S)^2(W(z_S)^2 - 2\tilde{W}_j(z_S)^2)^{(m_j+n_j-1)/2}}{(W(z_S)^2 + 2\tilde{W}_j(z_S)^2)^{(m_j+n_j+3)/2}} m_j!!(n_j-1)!! & (\text{if } m_j \text{ odd and } n_j \text{ even,}) \\ 0 & (\text{otherwise,}) \end{cases} \quad (\text{S16})$$

where $!!$ denotes the double factorial, with the special case that $(-1)!!$ is interpreted to mean 1.

[S1] Erwin Feldheim, Développements en série de polynômes d'Hermite et de Laguerre à l'aide des transformations de Gauss et de Hankel, I-III, Kon. Nederlandsche Akad. van Wet. Proceedings **41**, 224 (1940).